Supplementary materials for: *Quantum interference between quasi-2D Fermi surface sheets in UTe_2*

1 SAMPLE CHARACTERIZATION AND MEASUREMENT

We performed contactless resistivity measurements utilizing the tunnel diode oscillator (TDO) [1] and proximity detector oscillator (PDO) [2, 3] techniques. For both TDO and PDO, the measurement concerns the change in frequency f of an LC circuit connected to a coil that is coupled to a UTe_2 sample in such a manner as to achieve a high effective filling factor η. As the applied magnetic field is swept, changes in the resistivity ρ and susceptibility χ of the sample are manifested by the changing inductance of the measurement coil. This in turn leads to a frequency shift of the LC circuit, which may be captured by the equation

$$\frac{\Delta f}{f} \approx -\eta \frac{\delta}{d}\left(\mu_r \frac{\Delta\rho}{\rho} + \Delta\chi_s\right), \tag{1}$$

where d is the sample thickness, $\mu_r = \chi_s + 1$, and the skin depth $\delta = \sqrt{\frac{2\rho}{\mu_r \mu_0 \omega}}$, with excitation frequency ω [2, 3]. This sensitivity of Δf to δ generally leads to Δf being dominated by changes in χ in insulating materials (characterized by high ρ and long δ), whereas in good metals like UTe_2 it is dominated by the change in ρ. Accordingly, the PDO and TDO techniques are often referred to as a contactless resistivity measurement, for implicit cases of measurements on high conductivity materials.

While the operation of both is fundamentally premised on Eqn. 1, each of the TDO and PDO techniques have their own subtle advantages and disadvantages. While TDO generally achieves greater measurement fidelity than PDO, to operate it requires a low line impedance between the measurement coil and the tunnel diode [1]. It is thereby complicated by the necessity to include some electronic components in close proximity to the sample (i.e. inside the cryostat). By comparison, all PDO electronics can be located outside the cryostat, making optimization of signal to noise easier to perform without having to remove and subsequently re-load the sample. We deployed a TDO setup in steady (dc) magnet systems, similar to the procedure of e.g. ref. [4], and PDO in pulsed magnets, similar to e.g. refs. [5, 6].

High quality UTe_2 samples grown in a molten salt flux (MSF) were selected for quantum oscillation studies, each of which exhibited singular superconducting transitions in specific heat capacity measurements indicative of high purity crystals (Figure S1). We identify the T_c as 2.1 K, measured by the onset of diamgnetism in magnetization measurements. From the specific heat of this sample we calculate its normal state Sommerfeld coefficient, γ_N, to be 123.23(10) $\text{mJK}^{-2}\text{mol}^{-1}$ and the change in specific heat at the onset of superconductivity, ΔC, to be 235.0 $\text{mJK}^{-2}\text{mol}^{-1}$. From this we determine that $\Delta C/\gamma_N \approx 1.91$, well beyond the weak coupling BCS limit of 1.43. Previous studies have shown that $\Delta C/\gamma_N$ increases with sample quality, where the highest $\Delta C/\gamma_N$ for chemical vapor transport (CVT)

samples has been reported to be 1.8 [7]. This further evidences the high-quality of the MSF samples used in this work.

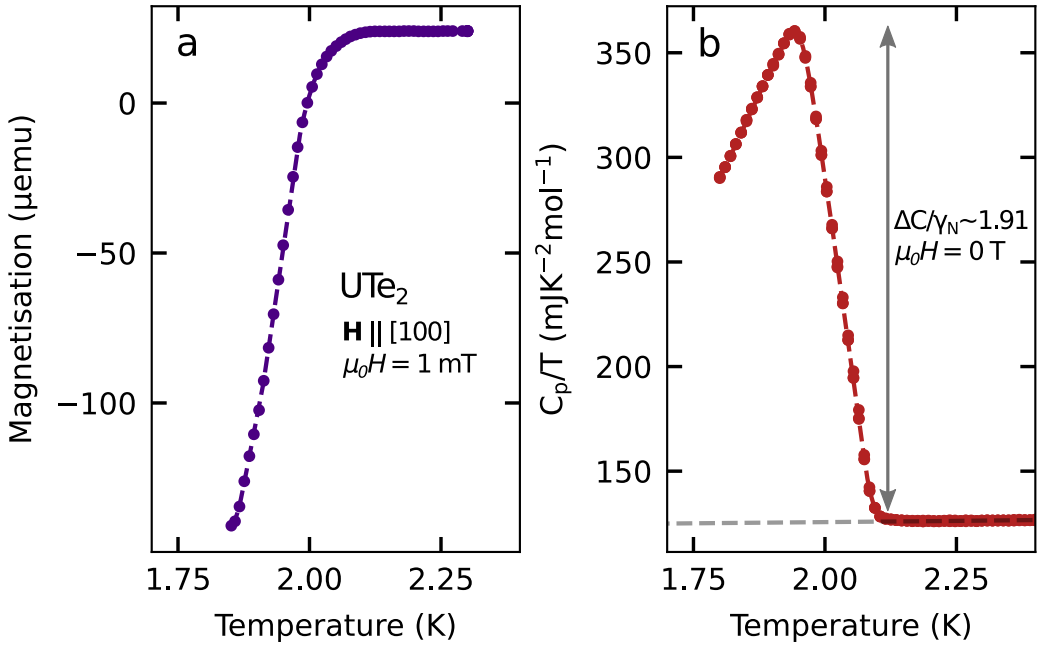

Figure S1: (a) Magnetisation versus temperature in a small applied field of 1 mT measured on the same sample as that for which QIO data are presented in the main text. Diamagnetism onsets at 2.1 K, from which we identify T_c. (b) Specific heat capacity of the same sample showing a sharp, singular transition at the onset of superconductivity.

In order to perform contactless resistivity measurements via either the TDO or PDO technique, samples were placed either inside cylindrical (tank) coils wound around the sample, or on top of planar coils (Figure S2a). Consistent data were obtained from both choices of coils. However, the choice of which type of coil to deploy in certain environments can considerably affect the resolved signal to noise for quantum oscillations.

The use of planar coils provides two benefits:

1. Firstly, this allows for measurements of a single sample in both pulsed-field and dc-field measurements, without having to change the coil. In pulsed fields a planar coil is desirable, as a compensation loop is easily wound, in order to minimise dB/dt through the entire coil as the field is rapidly increased and decreased thereby minimising the pick-up of the field itself (and thus maximising the sensitivity to the sample) [8].

2. Secondly, using a planar coil allows a Lauegram of the sample to be taken after it has been mounted, ensuring good knowledge of the sample alignment (Figure S2b).

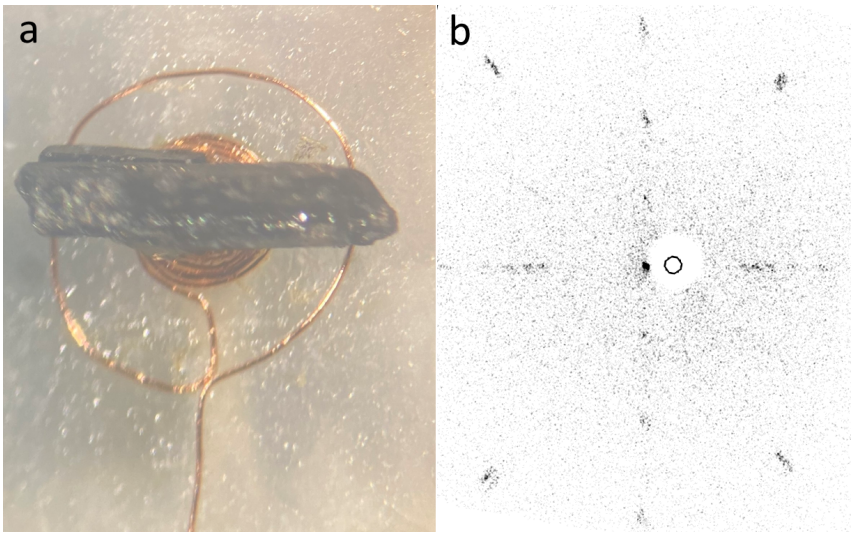

Figure S2: (a) Sample of high quality UTe_2 mounted on a planar coil. The c-axis is into the page, with the a-axis running left–right, b-axis up–down. (b) Lauegram of the sample in panel (a) taken once it had been mounted on the coil. The measured spectrum is in good agreement with the expected c-axis spectrum, with no extraneous peaks observed.

2 LIFSHITZ-KOSEVICH ANALYSIS FOR H || [001]

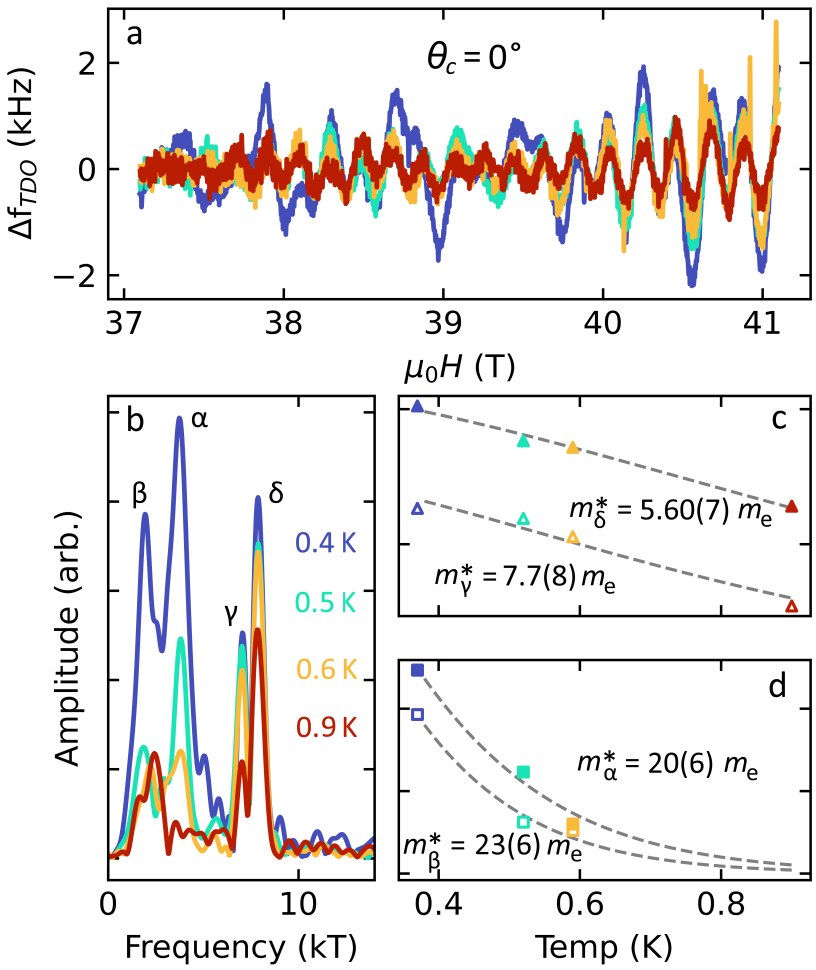

Figure S3: (a) Background-subtracted contactless resistivity of UTe_2 as measured along the c-axis in the field range 37–41 T at incremental temperatures as indicated. (b) The associated FFTs showing all four distinct frequencies at 2.4 kT, 3.9 kT, 7.9 kT, and 8.4 kT corresponding to the α, β, γ, and δ frequencies, respectively. Increasing temperature rapidly suppresses the α and β frequencies, whereas the γ and δ are more resilient to elevated temperatures due to their lighter apparent effective masses. (c-d) The Lifshitz-Kosevich temperature dependence of γ and δ shows that these higher frequencies are lighter in apparent effective mass whereas α and β are substantially heavier.

Observed oscillations for $\mathbf{H} \parallel [001]$			
Quantum interference frequencies		Quantum oscillation frequencies	
Frequency (kT)	Effective mass (m_e)	Frequency (kT)	Effective mass (m_e)
2.4	23(6)	3.5	41(2)
3.9	20(6)		
7.9	7.7(8)		
8.4	5.60(7)		

Table S1: Comparison between oscillatory components for $\mathbf{H} \parallel [001]$ observed in the magnetoconductance measured using TDO and those in the magnetisation measured by torque magnetometry [9]. We find that both the measured frequencies and masses are substantially different, demonstrating that these frequency branches measured by TDO are therefore very likely to be QIOs rather than QOs.

3 VARIABLE-FIELD STUDY

For magnetic field applied along the c-axis, the similarity in frequency expected for the α frequency, and the SdH signal expected for the actual cylindrical Fermi surface sheets [9], complicates the analysis of the TDO signal. By our Fermi surface model of the possible QI orbits in UTe_2, the α frequency is predicted to be at ≈ 3.9 kT, whereas the cyclotron orbits around the (degenerate) hole and electron sheets will produce a SdH frequency of ≈ 3.4 kT.

Data was analysed with a variable field range in order to determine the evolution of the frequency spectrum as a function of field, to delineate between oscillatory components that may be from conventional SdH QOs, and those that can only be explained as being QIOs (Figure S4).

Close to the c-axis, in the lowest field window of 36.0–39.5 T, the high-frequency γ and δ frequencies onset from ≈ 36 T, whereas the α QIO at 3.9 kT only begins to be observable at ≈ 38 T. In this field range, the β frequency is not observed. Alongside these QIOs, in the lowest field window, an FFT peak at 3.4 kT is clearly visible. This frequency is in good agreement with the dominant QO frequency branch we previously observed in dHvA and SdH measurements [9].

For $B \gtrapprox 40$ T, another QIO becomes observable at ≈ 2.9 kT, corresponding to the predicted β frequency. In this range, the 3.4 kT QO peak is only observable as a broadening of the 3.9 kT QIO. For increasingly higher field windows, the intensity of each peak in the QIO spectrum is enhanced whereas the 3.4 kT peak intensity does not increase, and becomes swamped by the QIOs.

The simultaneous measurement of all four predicted QIOs, as well as a frequency component that likely corresponds to a SdH QO orbit directly corresponding to the Fermi surface at lower fields, indicates that by limiting our analysis to the highest field ranges, the resolved oscillatory frequency spectrum corresponds to peaks from QIOs only. Therefore, this analysis provides good confidence that our discussion presented in the main text is relevant to the QIO frequency spectrum of UTe_2, and thereby provides valuable information pertaining to the Fermi surface geometry of this material.

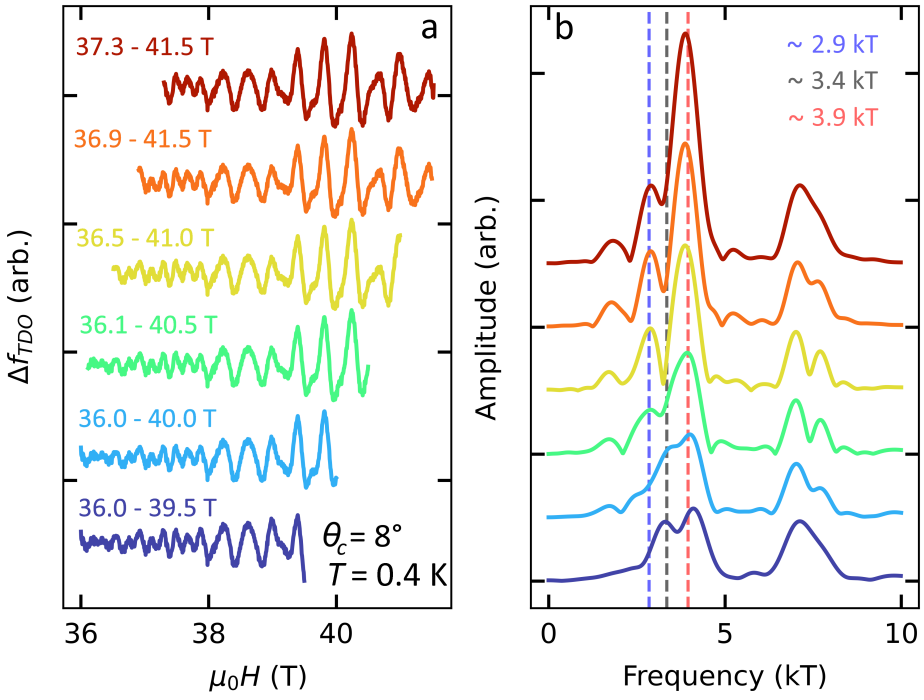

Figure S4: (a) Background-subtracted contactless resistivity signal over different field windows as indicated, showing the onset of different oscillatory components of the waveform. (b) The associated FFTs show that for 36.0 T $\leq B \leq$ 39.5 T a high frequency component is present, whereas the lower frequency oscillations only become well resolved for $B >$ 39.5 T. In this lower field range there appears to be two frequencies, one at $\approx$ 3.9 kT corresponding to a QIO, whereas there is also a clear peak at 3.4 kT which would be in good agreement with the conventional SdH QO orbit. As the field window is increased to around 41 T a new oscillatory frequency is observable at 2.9 kT, while the 3.9 kT frequency is enhanced at higher field ranges. This 2.9 kT oscillation is in good agreement with a predicted QIO frequency, and is also enhanced at increasing field ranges. Conversely, the 3.4 kT frequency component does not increase in amplitude as rapidly at high field.

4 EXCLUSION OF AN ALIEN PHASE AS A POSSIBLE ORIGIN OF THE OSCILLATORY SIGNAL

Given the notable differences between the oscillatory signals resolved in prior dHvA-effect experiments [9, 10] with those detected here by the TDO and PDO techniques, an important possibility to consider is whether this could be due to the inclusion of a small volume fraction of a metallic alien phase yielding SdH oscillations. It has been reported that the highest quality UTe_2 samples grown by the molten salt flux technique co-grow with the ferromagnetic semimetal U_7Te_{12}, with trace amounts of the ferromagnetic semiconductor U_3Te_5 also possible [11]. As U_7Te_{12} is hexagonal it tends to crystallize separately from UTe_2, but it is possible that trace amounts of U_7Te_{12} or U_3Te_5 may be present on the

surface of a UTe_2 single crystal. We note that a recent muon spin relaxation study of a mosaic of 24 molten salt flux-grown UTe_2 single crystals reported no signatures of alien phase inclusion [12]. However, it is of course important to rule out the possibility of quantum oscillations emanating from an alien phase, given the stark differences in masses and frequencies observed from TDO/PDO measurements compared to dHvA studies.

Firstly, any contribution from U_3Te_5 can be excluded as it is a semiconductor [13] and thus not expected to exhibit quantum oscillations as the Fermi surface will be gapped out at these low measurement temperatures. In this study, to obtain a good surface for mounting on planar coils, samples were cleaved to reveal a fresh (001) surface. This minimizes the possibility of any remnant impurity phase on an as-grown surface contributing to the measured signal, as the measurement is sensitive only to the cleaved surface section. While some oxidation of the cleaved surface is likely, the probability of an oxide layer being (i) metallic, (ii) single-crystalline, and (iii) exhibiting quantum oscillations for field oriented both parallel and perpendicular to the plane of the surface is remote. In Supplementary Section 7 we discuss the mean free path required to exhibit high frequency QIOs, underscoring the necessity to study high quality single crystals. Furthermore, we have observed QIOs in four separate samples in pulsed fields, two of which were also measured in static fields along with three other samples that were exclusively studied in static fields. All seven samples we have measured by TDO/PDO to high fields have exhibited consistent angular dependencies of the frequency spectra and corresponding effective masses. Thus, to be of an alien phase origin, the impurity phase would need to co-grow within the lattice of UTe_2 – which is highly unlikely for hexagonal U_7Te_{12}, or indeed for any other compound given that UTe_2 possesses a unique crystal structure [14].

Perhaps the strongest argument against an impurity origin comes from the dHvA studies of UTe_2 [9, 10]. Both the field modulation and torque magnetometry techniques are bulk-sensitive thermodynamic probes, which should capture the contribution of any impurity phases present. However, none have been identified. Samples from the same batch studied in our torque magnetometry study [9] were also measured in the present study, and give oscillatory magnetoconductance spectra consistent with samples from another growth batch and also with the oscillatory spectra reported in ref. [15]. This points strongly towards a quantum interference origin, due to the expectation of such frequencies only being observable in kinetic properties such as the electrical transport [16, 17]. As we discussed in the main text, the angular evolution of the oscillatory magnetoconductance of UTe_2 matches very well with our Fermi surface model (Fig. 4), and the oscillatory frequencies correspond very well with the expected areas enclosed by low-order MB networks. For these multiple reasons, we argue that a quantum interference origin is by far the most likely explanation for all of the oscillatory components of the magnetoconductance measured in this study; thus, we find that an alien impurity phase origin is extremely unlikely.

5 DETAILS OF QUANTUM INTERFERENCE ORBIT FREQUENCY CALCULATIONS

The effective area for each QIO can be determined according to Fig. 1 of the main text; the areas are effectively equal to the smallest loops enclosed by the outer surface of each cylinder. To model the QIOs upon rotating away from the c-axis, we start from the Fermi surface model of our earlier dHvA-effect QO study of UTe_2 [9]. Using this model, we define slicing planes between each cylinder along the directions of minimal k-space separation. Example bounding cylinders for the α and δ frequencies are shown in

Figure S5. Using this we obtain two new cylinders centered around the Γ and T points of the BZ. With these cylinders defined, we tessellate them in reciprocal space according to the periodicity of the BZ and then extract the extremal frequencies as would be done for conventional (dHvA or SdH) QOs. The Γ-centred cylinder is a neck and belly cylinder, which along the c-axis will produce frequencies of 8.1 kT and 7.2 kT, whereas the T-centered cylinder will generate frequencies of 3.9 kT and 2.7 kT.

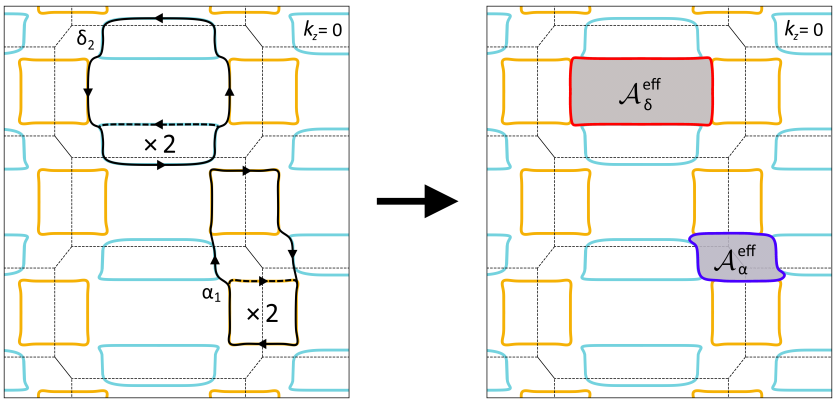

Figure S5: The quantum interference loops responsible for the α and δ frequencies and the corresponding bounding cylinders that were used to calculate their associated frequencies.

A similar analysis is much more difficult for the 220 T QIO and 4.5 kT breakdown orbit along the a-axis. Instead, we used the analytical form of our Fermi surface model to extract the frequencies. The 220 T QIO results from the interference between quasiparticles moving in the k_z direction on the electron and hole sheets (Figure 5 in the main text). The area corresponding to these oscillations is defined by the warping of the electron cylinder in the k_y direction as it moves away from, and back towards, the hole cylinder. The path of the hole cylinder in k_z as seen from down the a-axis is simply a vertical line, whereas the electron cylinder follows a sinusoidal path in k_y as a function of k_z. The amplitude of the displacement away from the hole cylinder can be defined as:

$$d_y = r_e(1 - \cos(k_z)) \tag{2}$$

where r_e is the degree of warping, which we determine to be 0.006 a_0^{-1} (where a_0 is the Bohr radius) from fitting our Fermi surface model [9]. Therefore the area of this loop can be determined as

$$A = \int_{-\pi}^{\pi} r_e(1 - \cos(k_z))dk_z = 2\pi r_e, \tag{3}$$

which corresponds to a QIO frequency of 206 T, in good agreement with the measured oscillatory frequency of 220 T.

The larger breakdown orbit can be modelled as an a ellipse in the k_y–k_z plane the with semi-major axes from $k_z = \pi/c = 0.120\ a_0^{-1}$ to $k_z = 0$ and $k_y = 0$ to $k_y = 0.087\ a_0^{-1}$ (Figure S6). The area of this orbit corresponds to a frequency of 4.9 kT, in reasonable agreement with the measured frequency of 4.5 kT.

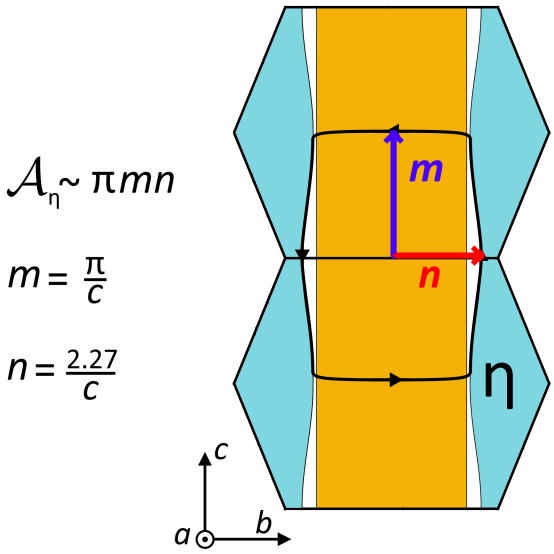

Figure S6: The semi-major axes of the ellipse used to calculate high frequency breakdown orbit η for magnetic field oriented along the a-axis.

We note that from this model by summing a combination of QO frequencies and QIO frequencies we can compare the addition of each area segment of the BZ with the actual area of the BZ itself, in the $k_z = \pi/2c$ plane, and subsequently corroborate whether or not this model is a good fit.

The frequency of a hypothetical orbit around the edge of the BZ in the $k_z = \pi/2c$ plane would be $\approx$ 16.5 kT. A full orbit around the BZ should be mathematically equivalent to

$$f_{tot} \approx f_{h^+} + f_{e^-} + f_\beta + (f_\gamma + f_\delta)/2. \tag{4}$$

Here f_{h^+} and f_{e^-} are the c-axis frequencies of the electron and hole cylinders, measured to be approximately 3.5 kT [9]. We have assumed that at $k_z = \pi/2c$ a hypothetical QIO frequency, which would account for the area around the gamma point surrounded by the hole and electron cylinders, may be approximated by the average of $f_\gamma + f_\delta$, namely the QIO frequencies at the $k_z = \pi/c$ and $k_z = 0$ points respectively. However, we note that this simple assumption introduces a level of uncertainty that is not insignificant. Nonetheless, we find that f_{tot} evaluates to 17.6 kT, which is in good agreement with the expected value of 16.5 kT to within the margin of error of this modelling.

6 DISAPPEARANCE OF A-AXIS QIOS

The disappearance of oscillations when the applied field was rotated away from the a-axis was seen in multiple samples, and for all samples measured, demonstrating the reproducibility of these results. This was found for the use of both planar coils and tank coils. In addition to the $a-c$ rotation plane shown in Fig. 5 of the main text, we find a similar effect in the $a-b$ rotation plane as well (Figure S7). This rapid

suppression of oscillation amplitude is inconsistent with these oscillations stemming from a 3D Fermi surface pocket.

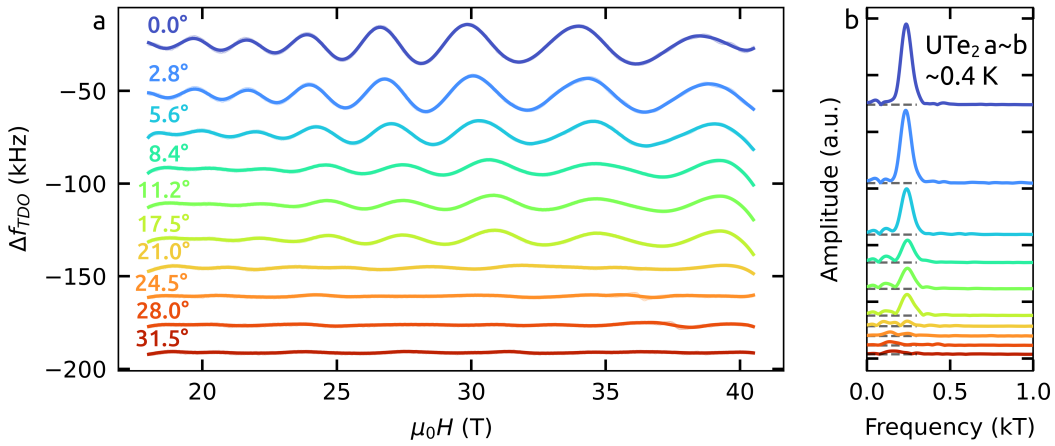

Figure S7: The angular dependence of QIOs when rotated away from the a-axis towards the b-axis. In this instance the QIOs were measured using the TDO technique with a tank coil.

7 CONSIDERATION OF QIO–IMPLIED MEAN FREE PATH

The frequency f of a QO from the dHvA or SdH effect observed at a magnetic field strength B can be directly related to the real space cyclotron radius r of the quasiparticle orbit giving rise to the QO. This may be written as

$$r = \sqrt{\frac{2\hbar f}{eB^2}}, \tag{5}$$

where $\hbar$ is the reduced Planck constant and e the elementary charge [18]. A simple estimate for the mean free path $l = 2r$, as in order for QOs to be manifested quasiparticles must be able to traverse a cyclotron orbit of this diameter without scattering.

In the case of QIOs, we can make a similar comparison. However, as discussed at length in the main text, QIO frequencies relate to the *difference* in reciprocal space area enclosed by the interfering quasiparticle paths – therefore the above argument above for evaluating l by considering QOs of frequency f only yields a lower bound for the magnitude of l that is necessary in order to observe QIOs (of the same frequency at the same B). Recalling Eqn. 1 of the main text, $\sum_{\lambda,\lambda'} \exp[i\left(\phi_\lambda - \phi_{\lambda'}\right)] = \sum_{\lambda,\lambda'} \exp\left(\frac{i\hbar}{eB}\mathcal{A}_{\lambda,\lambda'}\right)$ for phase ϕ and reciprocal space area $\mathcal{A}_\lambda$ enclosed by quasiparticle trajectory λ, by the Onsager relation [19] the corresponding QIO will have a frequency given by $f = \left|\frac{\hbar\mathcal{A}_\lambda}{2\pi e} - \frac{\hbar\mathcal{A}_{\lambda'}}{2\pi e}\right|$. Therefore, it is the longest of λ, λ' (i.e. the largest of $\mathcal{A}_\lambda$, $\mathcal{A}_{\lambda'}$) that is of relevance in considering l, as this trajectory must be successfully traversed (without scattering) in order for this frequency component to contribute to the conductivity.

In the case of the present study, of all the oscillatory frequency branches resolved by experiment the δ branch corresponds to the longest λ and thus largest $\mathcal{A}_\lambda$. For $\mathbf{H} \parallel [001]$ the observed frequency is 8.4 kT (Table S1). However, following the above argument we need to account for the effective subtraction of the component $\mathcal{A}_{\lambda'}$. Thus, to make a simple estimate of l in the spirit of Eqn. 5, the appropriate value of f to be used is 8.4 kT + 2 $\times$ 3.5 kT = 15.4 kT. For $B = 40$ T this yields $l = 2r = 230$ nm. We note that Eqn. 5 gives only a crude means by which to estimate l – a consideration of the Dingle damping factor [20] would be preferable, however the dependency of QIO amplitude on B, due to the exponentially enhanced probability of magnetic breakdown occurring with increasing B, complicates such an analysis. However, the simple arguments presented here underline the importance of studying high quality samples samples with long mean free paths when performing QIO studies. Furthermore, if high quality samples with large l values are available, the experimental study of QIOs can in certain cases be more attainable than a more conventional study of QOs – for example, if the effective masses are particularly large but can subtract to give much lighter QIOs that are observable to elevated temperatures [21].

References

[1] Craig T. Van Degrift. Tunnel diode oscillator for 0.001 ppm measurements at low temperatures. *Rev. Sci. Inst.*, 46(5):599–607, 09 2008.

[2] M. M. Altarawneh, C. H. Mielke, and J. S. Brooks. Proximity detector circuits: An alternative to tunnel diode oscillators for contactless measurements in pulsed magnetic field environments. *Rev. Sci. Inst.*, 80(6):066104, 2009.

[3] S Ghannadzadeh, M Coak, I Franke, PA Goddard, J Singleton, and Jamie L Manson. Measurement of magnetic susceptibility in pulsed magnetic fields using a proximity detector oscillator. *Rev. Sci. Inst.*, 82(11):113902, 2011.

[4] Konstantin Semeniuk, Hui Chang, Jordan Baglo, Sven Friedemann, Stanley W Tozer, William A Coniglio, Monika B Gamża, Pascal Reiss, Patricia Alireza, Inge Leermakers, et al. Truncated mass divergence in a Mott metal. *Proc. Natl. Acad. Sci. USA*, 120(38):e2301456120, 2023.

[5] B.J. Ramshaw, S.E. Sebastian, R.D. McDonald, J. Day, B.S. Tan, Z. Zhu, J.B. Betts, R. Liang, D.A. Bonn, W.N. Hardy, et al. Quasiparticle mass enhancement approaching optimal doping in a high-T_c superconductor. *Science*, 348(6232):317–320, 2015.

[6] H Liu, AJ Hickey, M Hartstein, AJ Davies, AG Eaton, T Elvin, E Polyakov, TH Vu, V Wichitwechkarn, T Förster, et al. f-electron hybridised Fermi surface in magnetic field-induced metallic YbB_{12}. *npj Quantum Mater.*, 7(1):12, 2022.

[7] Priscila F. S. Rosa, Ashley Weiland, Shannon S. Fender, Brian L. Scott, Filip Ronning, Joe D. Thompson, Eric D. Bauer, and Sean M. Thomas. Single thermodynamic transition at 2 K in superconducting UTe_2 single crystals. *Commun. Mater.*, 3(1):33, may 2022.

[8] F. F. Balakirev, T. Kong, M. Jaime, R. D. McDonald, C. H. Mielke, A. Gurevich, P. C. Canfield, and S. L. Bud'ko. Anisotropy reversal of the upper critical field at low temperatures and spin-locked superconductivity in $K_2Cr_3As_3$. *Phys. Rev. B*, 91:220505, 2015.

[9] A. G. Eaton, T. I. Weinberger, N. J. M. Popiel, Z. Wu, A. J. Hickey, A. Cabala, J. Pospíšil, J. Prokleška, T. Haidamak, G. Bastien, P. Opletal, H. Sakai, Y. Haga, R. Nowell, S. M. Benjamin, V. Sechovský, G. G. Lonzarich, F. M. Grosche, and M. Vališka. Quasi-2D Fermi surface in the anomalous superconductor UTe_2. *Nat. Commun.*, 15:223, 2024.

[10] Dai Aoki, Hironori Sakai, Petr Opletal, Yoshifumi Tokiwa, Jun Ishizuka, Youichi Yanase, Hisatomo Harima, Ai Nakamura, Dexin Li, Yoshiya Homma, Yusei Shimizu, Georg Knebel, Jacques Flouquet, and Yoshinori Haga. First Observation of the de Haas–van Alphen Effect and Fermi Surfaces in the Unconventional Superconductor UTe_2. *J. Phys. Soc. Jpn.*, 91(8):083704, 2022.

[11] H. Sakai, P. Opletal, Y. Tokiwa, E. Yamamoto, Y. Tokunaga, S. Kambe, and Y. Haga. Single crystal growth of superconducting $\mathrm{UTe_2}$ by molten salt flux method. *Phys. Rev. Materials*, 6:073401, 2022.

[12] N. Azari, M. Yakovlev, N. Rye, S. R. Dunsiger, S. Sundar, M. M. Bordelon, S. M. Thomas, J. D. Thompson, P. F. S. Rosa, and J. E. Sonier. Absence of Spontaneous Magnetic Fields due to Time-Reversal Symmetry Breaking in Bulk Superconducting $\mathrm{UTe_2}$. *Phys. Rev. Lett.*, 131:226504, Nov 2023.

[13] O. Tougait, M. Potel, and H. Noël. Crystal Structure and Magnetic Properties of the Binary Triuranium Pentatelluride U_2Te_5. *J. Solid State Chem.*, 139(2):356–361, 1998.

[14] Dexin Li, Ai Nakamura, Fuminori Honda, Yoshiki J Sato, Yoshiya Homma, Yusei Shimizu, Jun Ishizuka, Youichi Yanase, Georg Knebel, Jacques Flouquet, et al. Magnetic properties under pressure in novel spin-triplet superconductor UTe_2. *J. Phys. Soc. Jpn.*, 90(7):073703, 2021.

[15] Christopher Broyles, Zack Rehfuss, Hasan Siddiquee, Jiahui Althena Zhu, Kaiwen Zheng, Martin Nikolo, David Graf, John Singleton, and Sheng Ran. Revealing a 3D Fermi Surface Pocket and Electron-Hole Tunneling in $\mathrm{UTe_2}$ with Quantum Oscillations. *Phys. Rev. Lett.*, 131:036501, 2023.

[16] M. V. Kartsovnik, G. Yu. Logvenov, T. Ishiguro, W. Biberacher, H. Anzai, and N. D. Kushch. Direct Observation of the Magnetic-Breakdown Induced Quantum Interference in the Quasi-Two-Dimensional Organic Metal κ-$(\mathrm{BEDT\text{-}\ TTF})_2\mathrm{CU(NCS)_2}$. *Phys. Rev. Lett.*, 77:2530–2533, 1996.

[17] N Harrison, J Caulfield, J Singleton, PHP Reinders, F Herlach, W Hayes, M Kurmoo, and P Day. Magnetic breakdown and quantum interference in the quasi-two-dimensional superconductor κ-(BEDT-TTF)$_2$Cu(NCS)$_2$ in high magnetic fields. *J. Phys.: Condens. Matter*, 8(29):5415, 1996.

[18] D Shoenberg. *Magnetic Oscillations in Metals*. Cambridge University Press, Cambridge, UK, 1984.

[19] L. Onsager. Interpretation of the de Haas-van Alphen effect. *Philos. Mag.*, 43(344):1006–1008, 1952.

[20] R. B. Dingle. Some magnetic properties of metals II. The influence of collisions on the magnetic behaviour of large systems. *Proc. R. Soc. Lond. A*, 211(1107):517–525, 1952.

[21] T. I. Weinberger, Z. Wu, A. J. Hickey, D. E. Graf, G. Li, P. Wang, R. Zhou, A. Cabala, J. Pu, V. Sechovsky, M. Valiska, G. G. Lonzarich, F. M. Grosche, and A. G. Eaton. Pressure-enhanced f-electron orbital weighting in UTe_2 mapped by quantum interferometry, arXiv:2403.03946, 2024.